In Situ TEM Studies of Micron-sized All-solid-state Fluoride Ion Batteries: Preparation, Prospects, and Challenges

MOHAMMED HAMMAD FAWEY,[1,2] VENKATA SAI KIRAN CHAKRAVADHANULA,[1,2,3,4]*
MUNNANGI ANJI REDDY,[1,3] CARINE RONGEAT,[1] TORSTEN SCHERER,[1,4] HORST HAHN,[1,2,3]
MAXIMILIAN FICHTNER,[1,3] AND CHRISTIAN KÜBEL[1,3,4]

[1]*Institute of Nanotechnology (INT), Karlsruhe Institute of Technology (KIT), Hermann-von-Helmholtz-Platz 1, 76344 Eggenstein-Leopoldshafen, Germany*
[2]*Joint Research Laboratory Nanomaterials (KIT and TUD) at Technische Universität Darmstadt (TUD), Jovanka-Bontschits-Str. 2, Darmstadt 64287, Germany*
[3]*Helmholtz Institute Ulm for Electrochemical Energy Storage (HIU), Karlsruhe Institute of Technology (KIT), Helmholtzstr. 11, Ulm 89081, Germany*
[4]*Karlsruhe Nano Micro Facility (KNMF), Karlsruhe Institute of Technology (KIT), Hermann-von-Helmholtz-Platz 1, 76344 Eggenstein-Leopoldshafen, Germany*

ABSTRACT   Trustworthy preparation and contacting of micron-sized batteries is an essential task to enable reliable in situ TEM studies during electrochemical biasing. Some of the challenges and solutions for the preparation of all-solid-state batteries for in situ TEM electrochemical studies are discussed using an optimized focused ion beam (FIB) approach. In particular redeposition, resistivity, porosity of the electrodes/electrolyte and leakage current are addressed. Overcoming these challenges, an all-solid-state fluoride ion battery has been prepared as a model system for in situ TEM electrochemical biasing studies and first results on a $Bi/La_{0.9}Ba_{0.1}F_{2.9}$ half-cell are presented. *Microsc. Res. Tech. 79:615–624, 2016.* © 2016 Wiley Periodicals, Inc.

INTRODUCTION

Affordable, reliable, and safe electrochemical energy storage systems are required for a wide variety of applications such as hybrid and electric vehicles (Belharouak et al., 2011; Han et al., 2014; Smith et al., 2012), stationary systems (Purvins and Sumner, 2013; Takami et al., 2013; Wagner, 2007; Xu et al., 2010), notebook computers (David, 2001; Warner, 2015), or also for spacecrafts (Marsh et al., 2001; Nishizawa et al., 2013). A large number of groups worldwide are working to develop an understanding of the local processes that occur during the charging/discharging of such storage systems with the main purpose of optimizing efficiency, power density, and life-time. A plethora of characterization tools are used with the possibility to carry out in situ and in operando studies of energy storage systems (Fell et al., 2012; Hardwick et al., 2007; Harks et al., 2015; Mansour et al., 2010; Nonaka et al., 2001; Ramdon et al., 2014; Sagane et al., 2013; Shao, 2014). Presently, lithium ion batteries (LIBs) are the systems most studied and industrially relevant among the battery systems. Future developments and performance optimization of batteries depend critically on understanding the electrochemical reactions and degradation processes taking place during cycling. Therefore, in situ studies of electrochemical processes are necessary to follow the structural transformations during cycling using various characterization techniques, e.g. optical microscopy (Beaulieu et al., 2001; Rosso et al., 2006), scanning electron microscopy (Chen et al., 2011; Orsini et al., 1998), transmission electron microscopy (Huang et al., 2010; Liu and Huang, 2011; Yamamoto et al., 2010), X-ray (Hatchard and Dahn, 2004; Li and Dahn, 2007; Obrovac and Christensen, 2004), neutron diffraction (Roberts et al., 2013; Sharma et al., 2010; Petibon et al., 2015), nuclear magnetic resonance spectroscopy (Bhattacharyya et al., 2010; Key et al., 2009, 2011), and Raman spectroscopy (Hardwick et al., 2008; Long et al., 2011). Among these techniques, in situ TEM provides the highest spatial resolution to directly visualize dynamic processes following morphological changes along with structural and chemical changes. In situ TEM studies require complex sample geometries to, on one hand, fulfill the stringent requirements for reliable TEM analysis and, on the other hand, to provide the right environment for reliable observation of chemical reactions to correlate the structural changes with the actual operating conditions. A variety of TEM sample holders have been developed over the last couple years to approach an environment closely mimicking the actual operation conditions of batteries (Bernal et al., 2015; Eswara Moorthy et al., 2013; Miller et al., 2015; Uhlig et al., 2003) inside a TEM. Despite this, the preparation of an actual battery system and developing or employing

the right imaging conditions, to prevent preparation and beam induced artifacts still remains a challenge.

As an alternative to Li-ion batteries, alternative technologies are investigated based on different chemistries using, e.g., sodium, magnesium or chloride ions for charge transport in secondary batteries. Batteries based on a fluoride ion shuttle (fluoride ion battery) are an interesting alternative to Li-ion batteries as they can theoretically provide substantially higher volumetric energy densities compared to Li-ion batteries. Recently, the principle of a secondary battery based on a fluoride ion shuttle has been demonstrated (Reddy and Fichtner, 2011). In addition, LIBs are generally operated under (semi) inert conditions, as the individual components (cathode, anode and electrolyte) are typically air/moisture sensitive. For in situ TEM studies, in most cases, liquid electrolytes are used with specialized in situ liquid TEM electrochemical sample holders. However, recent studies (Abellan et al., 2014; Gu et al., 2013; Leenheer et al., 2015; Woehl et al., 2012) have shown that liquid electrolytes are very sensitive to the electron beam as well as most of the Li-rich electrode materials, thereby rendering it difficult to separate electron beam induced damage/ changes and electrochemical effects during cycling. Hence, an ideal battery system for in situ TEM studies is one without the aforementioned critical aspects, enabling to study only the dynamic processes due to electrochemical cycling. For this purpose, the recently developed fluoride ion battery (Reddy and Fichtner, 2011) is a good model system. The individual components are not particularly air-sensitive and are stable under the electron beam. A micron-sized all solid-state fluoride-ion cell can be fabricated by FIB with a geometry closer to the bulk cell setup compared to other in situ TEM setups based on individual nanowires contacted by an ionic liquid (Liu and Huang, 2011; Liu et al., 2012; Su et al., 2013a,b; Wang, 2014; Xie et al., 2014; Zamfir et al., 2013). Here, we show the sample preparation of an all-solid-state fluoride ion battery accompanied by in situ TEM studies of a half-cell fluoride ion battery as a first step to follow and understand the detailed electrochemical processes in fluoride ion batteries.

MATERIALS AND METHODS

The fabrication of a micron-sized cell from an all-solid-state battery for in situ characterization is realized by using focused ion beam techniques (FIB). The starting full cell in pellet form consisting of cathode, anode and solid electrolyte was pressed at 5 GPa from powders (Fig. 1a). The pellet was prepared using a composite of Mg, MgF$_2$, C, and La$_{0.9}$Ba$_{0.1}$F$_{2.9}$ as anode, a composite of Cu and C as cathode and La$_{0.9}$Ba$_{0.1}$F$_{2.9}$ as solid electrolyte. Both composites were prepared by ball-milling of the corresponding compounds (Rongeat et al., 2014). La$_{0.9}$Ba$_{0.1}$F$_{2.9}$ was prepared according to the method by M. Anji Reddy and M. Fichtner (Reddy and Fichtner, 2011). The pellet for the battery testing was prepared by assembling the powders in layers, followed by compacting them. The thickness of the solid electrolyte was chosen around 20–30 μm to prevent local short-circuits. The micron-sized battery is milled by FIB from the bulk battery and then mounted on a MEMS device (Meng et al., 2011) with electrical Pt
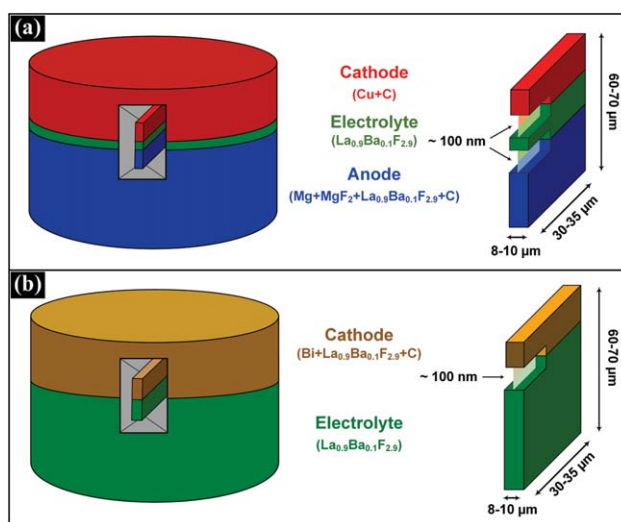

Fig. 1. Schematic of the all-solid-state battery and FIB preparation of a cross section (**a**) full cell, (**b**) half-cell. [Color figure can be viewed in the online issue, which is available at wileyonlinelibrary.com.]

contacts on a SiN membrane. The micron-sized battery is finally contacted by local Pt-deposition between the electrical contacts and the anode/cathode materials to enable electrochemical biasing. In addition, a half-cell (Fig. 1b) is prepared analogously based on a Bi, C and La$_{0.9}$Ba$_{0.1}$F$_{2.9}$ composite as cathode and La$_{0.9}$Ba$_{0.1}$F$_{2.9}$ acting both as electrolyte and fluoride ion source for the in situ cell operation.

In this article, we describe the fabrication procedure and discuss challenges like contamination during metal deposition and porosity of the battery materials. Large TEM lamellae with dimensions of ∼70 × 35 × 10 μm^3 were milled incorporating the interfaces (Anode-Electrolyte and Cathode-Electrolyte in case of the full cell, Cathode-Electrolyte in case of the half-cell) using conventional FIB TEM lamella preparation methods (Jublot and Texier, 2014; Kuwano et al., 2008; Mayer et al., 2007) (Figs. 2 and 3). The preparation was initially performed at 30 kV with an ion beam current of 20 nA, followed by cleaning at 6.5 nA ion-beam current. This milled battery lamella was then mounted on a Cu lift-out grid on a flip stage using an Omniprobe 200 system. The areas of interest, the aforementioned interfaces, were thinned to about 100 nm thickness. The final thinning steps were performed at 5 kV with 0.15 nA ion beam current. Afterwards, the thinned battery lamella was transferred onto a MEMS device (Protochips E-AEK11). For loading, the TEM lamella mounted on the flip stage was tilted 90° and transferred using the Omniprobe micromanipulator onto the MEMS device. Prior to the transfer, two Pt columns with dimensions of ∼1.5 × 1.5 × 4 μm^3 are prepared on the contacts of the MEMS device by ion beam induced deposition (IBID) to support and facilitate the mounting process. The IBID parameters were 30 kV acceleration voltage, 48 pA current and 200 ns dwell time. Afterwards, the micron-sized cell is contacted by local Pt-deposition between the electrical contacts of the MEMS device and the electrodes of the cell to enable electrochemical biasing (Figs. 3a and 3c).
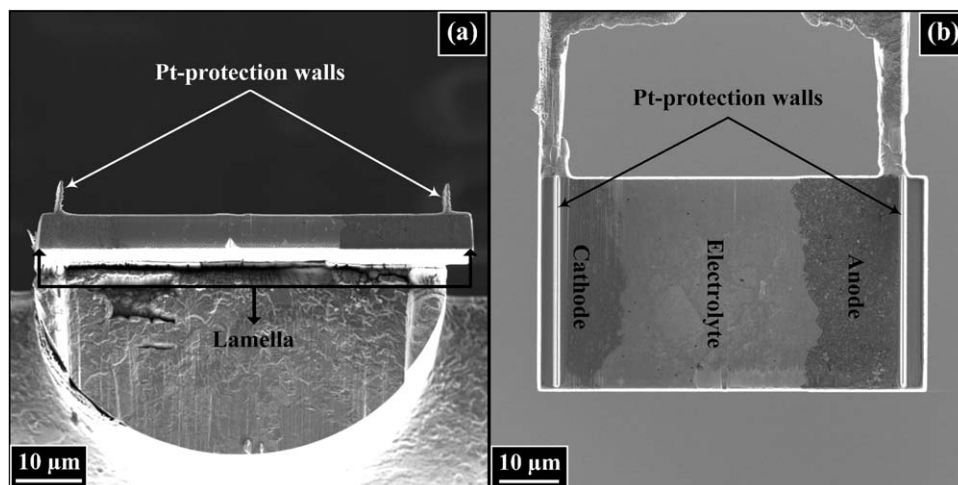
Fig. 2. Battery lamella on the copper grid, (**a**) side view after deposition the two Pt-protection walls, (**b**) top view after initial thinning.
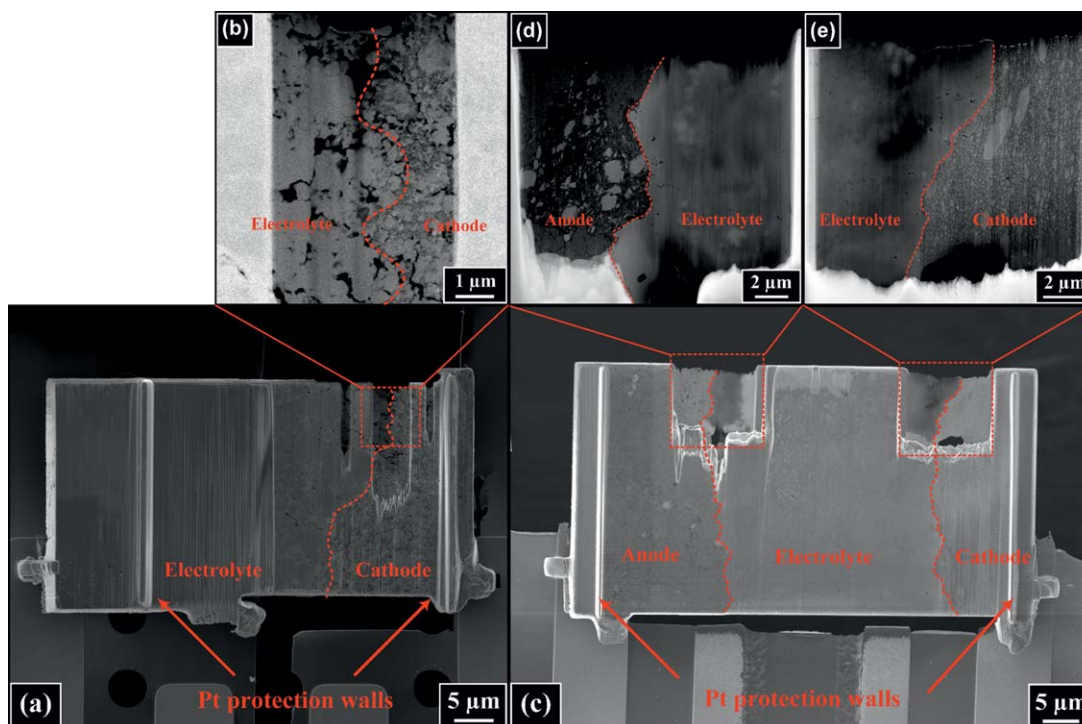

Fig. 3. (**a**) SEM image of the micron-size half-cell mounted on the MEMS device, (**b**) STEM image of the thin area at cathode/electrolyte interface of the half-cell, (**c**) SEM image of the micron-sized full-cell mounted on the MEMS device, (**d** and **e**) STEM images of the thin areas at interfaces of the full cell. [Color figure can be viewed in the online issue, which is available at wileyonlinelibrary.com.]

RESULTS AND DISCUSSION

During the various stages of the sample preparation of a battery for in situ TEM investigation, a variety of challenges arise to successfully produce an operational battery sample, e.g. the porous nature of the pellets, contamination during metal deposition, contact resistance and leakage currents. These aspects are pivotal for the successful operation of an in situ biasing experiment and are discussed in detail for the electrochemical biasing studies on the fluoride battery.

Porosity of the Battery Materials

Generally, in a bulk battery, the ball-milled composite components for anode and cathode require an optimum porosity to enable compensation of volumetric changes during electrochemical cycling. However, for in situ TEM measurements, which require a thin
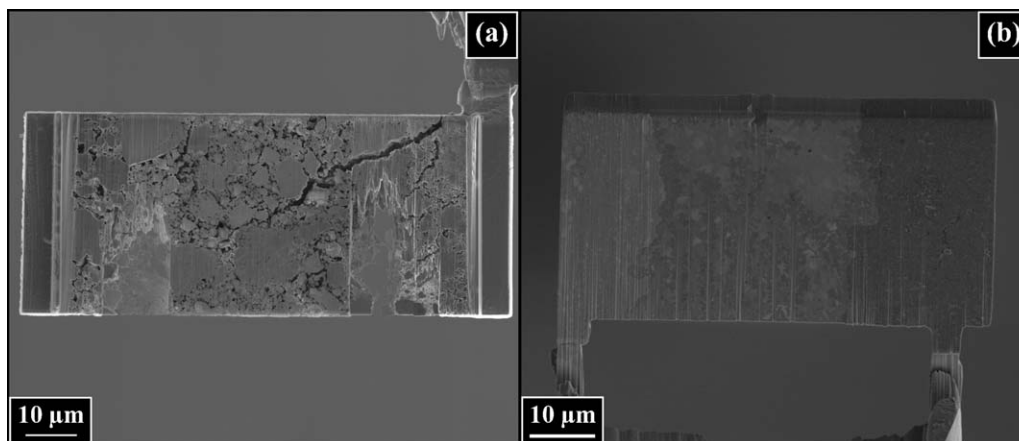
Fig. 4. (**a**) Cracks during lifting-out and thinning of a TEM lamellae from a porous battery (**b**) lamella after pressing at 5 Gpa for 5 min.

lamella, porosity poses a huge problem affecting both the mechanical stability and the interface-connectivity in the electron transparent region of the battery lamella. A compromise between porosity and stability/conductivity of the battery-lamella is required for a successful in situ TEM study. To obtain the required porosity, the initially assembled powder based batteries were further compressed at a pressure of ∼5 GPa for ∼5 min to produce a stable, dense battery with good contact between neighboring grains as well as between the electrodes and electrolyte (Fig. 4).

Contamination during Metal Deposition

Contamination of the battery lamella during electrical contacting by Pt (or also W) deposition is a major problem during FIB preparation (Duchamp et al., 2014; Nan and Lung, 2013). Figures 5a–5d shows the deposition of Pt and W "wires" with nominal dimensions of 25 μm (length) × 1 μm (width) × 1 μm (height) using ion beam induced deposition (IBID) and electron beam induced deposition (EDID) inside the FIB. Both the Pt and the W wires were deposited using the following parameters: current 1.6 nA, acceleration voltage 5 kV and dwell time 1.4 ms (EBID) and current 46 pA, acceleration voltage 30 kV and dwell time 200 ns (IBID). In addition to the predefined areas for the wire, deposition outside the wire is visible as bright halos. For both the Pt and the W deposition the contamination area around the wires was smaller for EBID (∼1 μm) compared to IBID (∼17 μm Pt, ∼3.5 μm W). For conventional TEM sample preparation, this is not critical, but for the in situ sample preparation, this metal deposition might create an electrical contact between the electrodes resulting in a short circuit of the micron-sized battery. The probability of this to happen is much higher, if the size of the battery is small. Preventing this is a prerequisite to obtain a functional battery. Consequently, a MEMS (Protochips, E-AEK11) device with a wide separation between the Pt contacts has to be used (50 μm, in the present case).

As an additional approach to reduce the metal contamination during electrical contacting of the battery, two Pt walls were deposited on cathode and anode before performing the initial thinning. This aims to reduce the flow across the active area of the battery and thus contamination/redeposition. The Pt-protection walls were deposited vertically on the lamella (Fig. 2a) and are about 300 nm wide and 7 μm high. After the deposition of the Pt-protection walls, the area between the two Pt-protection walls was cleaned using the Ga ion beam to remove any metal deposition on the complete battery. This was performed before thinning the area of interest at the interfaces between the electrodes (Fig. 2b). With this process we reduce metal contamination and redeposition during the later sample preparation stages. The Pt protection walls were used to protect the micron-sized battery from residual deposition during the contacting. In addition, removing the SiN membrane between the contacts also helped to reduce contamination by allowing free gas flow (Precursor gas from the Gas Injection System, GIS) from the GIS around the sample (Duchamp et al., 2014).

Contact Resistance

The conductivity of the metal contacts has to be sufficiently high to prevent significant losses at the contacts during the charging/discharging process of the micro battery. Therefore, it is important to know the resistivity of the metal deposited from the GIS on the MEMS device. The aforementioned Pt and W structures deposited by IBID and EBID were used to measure and compare the resistivity of the resulting metal wires (Fig. 6). A Keithley 2611A power supply with a Protochips Aduro 200 in situ electrical TEM sample holder was used running a voltage sweep of 100/150 mV and measuring the corresponding current. The resistance of Pt deposited by EBID is 6 orders of magnitude higher compared to that deposited by IBID (1.88 MΩ and 156 Ω, Figs. 6a and 6b). A similar difference was observed for W, where the resistance was 0.135 MΩ and 95 Ω for EBID and IBID respectively (Figs. 6c and 6d). Based on the nominal wire geometry, the resistivity of Pt is calculated to be 7.5×10^{-2} $\Omega \text{ m}^{-1}$ (EBID) and 6.2×10^{-6} $\Omega \text{ m}^{-1}$ (IBID), in agreement with previously reported results (Botman et al.,
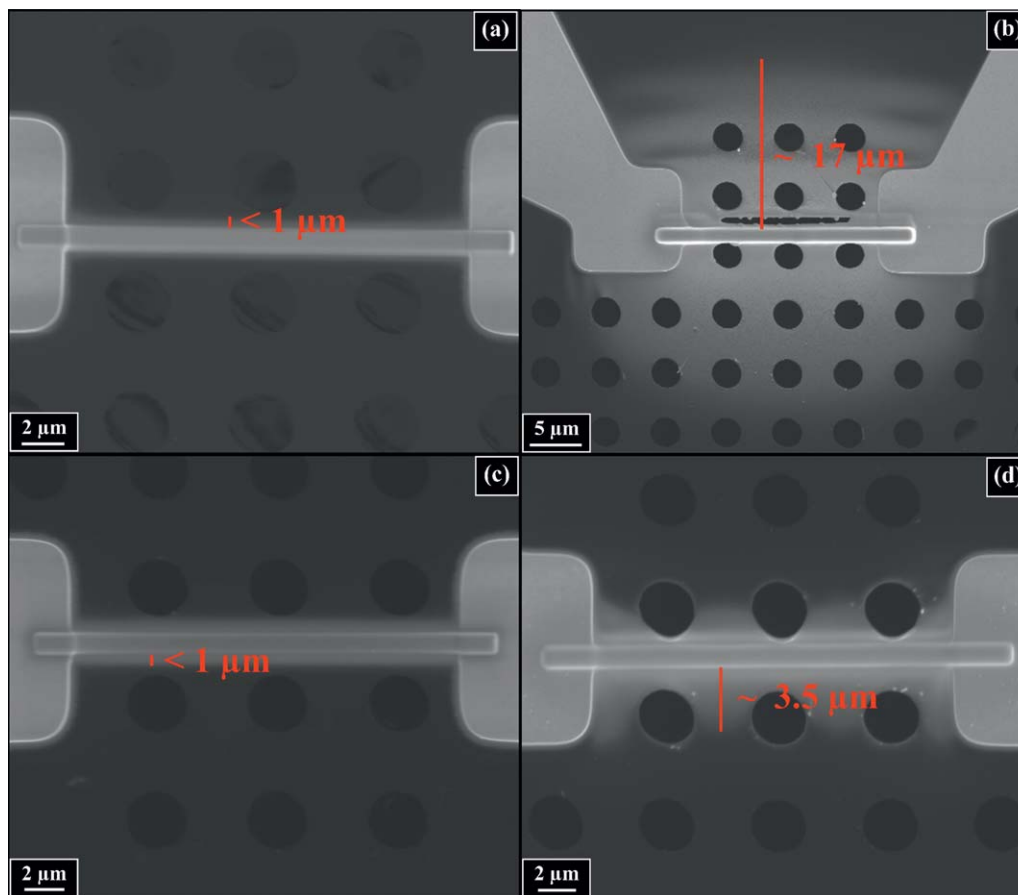
Fig. 5. (**a**) Pt deposited by e-beam, (**b**) Pt deposited by ion beam, (**c**) W deposited by e-beam, (**d**) W deposited by ion beam. [Color figure can be viewed in the online issue, which is available at wileyonline library.com.]

2008; Brunel et al., 2011; Fernández-Pacheco et al., 2009; Lin et al., 2003; Mulders, 2014; Reguer et al., 2008; Teresa et al., 2009; Vaz et al., 2008). The resistivity of the W is 5.4×10^{-3} Ω m^{-1} (EBID) and 3.8×10^{-6} Ω m^{-1} (IBID), also in agreement with previously reported results (Horváth et al., 2006; Kanzaki et al., 2011; Li and Warburton, 2007; Li et al., 2008, 2012; Prestigiacomo et al., 2004; Reguer et al., 2008). The resistance difference between the IBID and EBID techniques can be partially attributed to differences in the carbon content incorporated from the precursor system into the wires in addition to some gallium incorporation (Jenkins et al., 1999; Koh, 1991; Langfischer et al., 2002; Li et al., 2006; Melngailis, 1991). Moreover, there are other potential effects that could influence the conductivity such as density, where the IBID wires are more denser than that deposited by EBID (Tham et al., 2006), and also cross-linkage/carbonization level of the residual carbon or gallium incorporation. However, it is expected that the high carbon content is the main factor changing the wire structure from a percolating Pt or W network to isolated metal nanoparticles, so that the conductivity switches from a metallic conductivity to a "hopping" process.

Based on a SEM-EDX analysis, the Pt-IBID wire consists of ~64 at% Pt and ~36 at% Ga with carbon below the detection limit, while the Pt-EBID wire consists of ~36 at% Pt and ~64 at% C. This Pt content is higher than reported previously (Li et al., 2006; Lin et al., 2003, 2004). As the electrical and structural properties of the IBID or EBID deposited wires depend on a number of factors such as beam current and energy (Hoyle et al., 1994; Platen et al., 1992), scanning conditions (Hiroshima and Komuro, 1997; Hoyle et al., 1993), vacuum conditions (Utke et al., 2008) and the precursor compound (Utke et al., 2008), it is not surprising that the composition varies somewhat between different setups. For the W-IBID wire we measured ~44 at% W, ~18 at% Ga and ~38 at% O with carbon below the detection limit, while the W-EBID wire consists of ~23 at% W, ~33 at% C and ~43 at% O. The oxygen content in the W wires can be attributed either to the rest gas in the vacuum system (Melngailis, 1991), insufficient decomposition of the $W(CO)_6$ precursor (Koh, 1991), or oxidation when removing the test structure from the FIB.

For contacting the lamella on the MEMS device, two Pt contacts with dimensions of 5 μm (length) × 2 μm (width) × 1 μm (height) were used. The resistance of two contacting Pt-EBID wires would be 375 kΩ, while it is only 31 Ω in the case of Pt-IBID. This resistance from the Pt-IBID structure is negligible compared to the resistance the whole micron-sized battery (~1 MΩ), whereas the Pt-EBID wires would have added

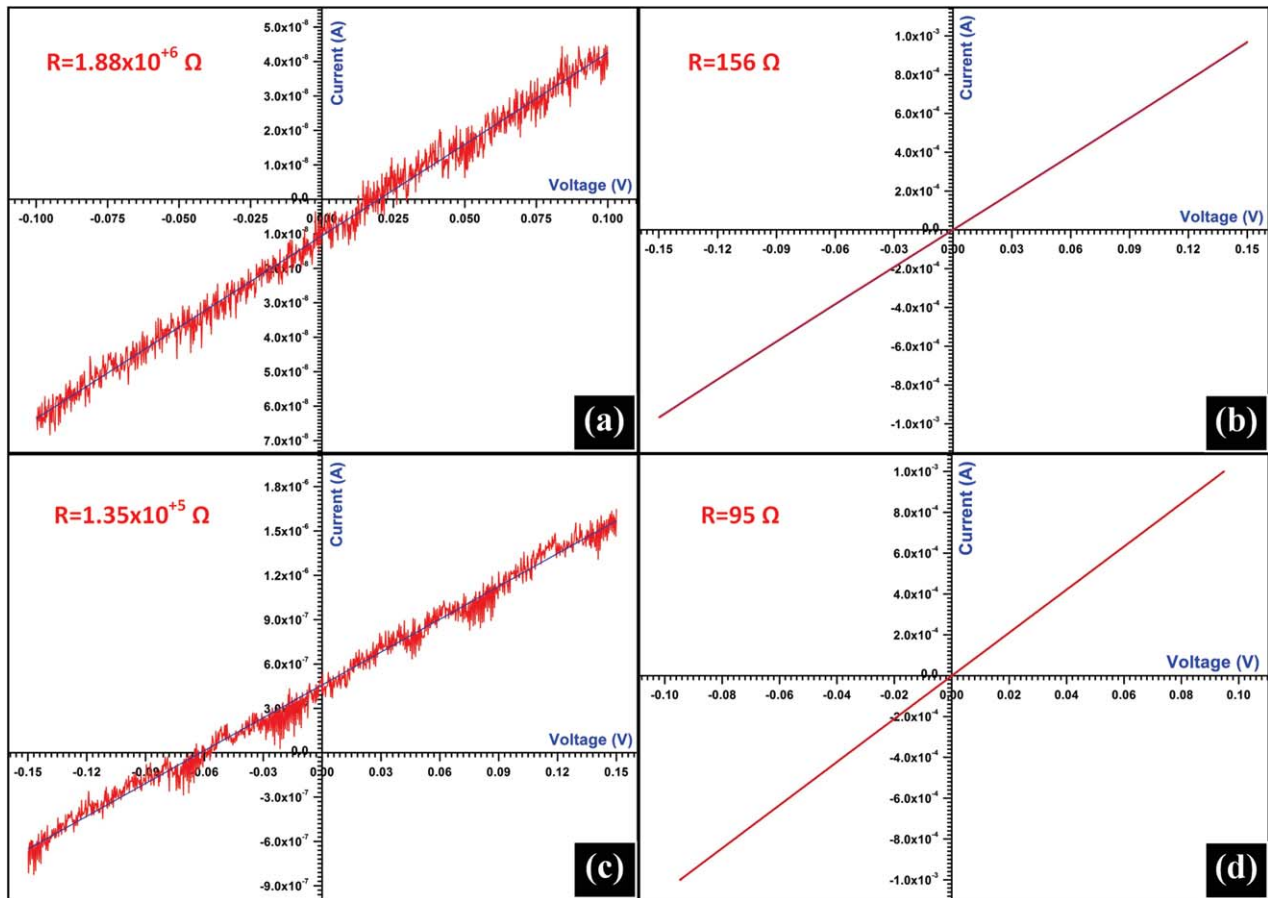Fig. 6. I–V curves and the resistance for (**a**) Pt deposited by e-beam, (**b**) Pt deposited by ion beam, (**c**) W deposited by e-beam, (**d**) W deposited by ion beam. [Color figure can be viewed in the online issue, which is available at wileyonlinelibrary.com.]
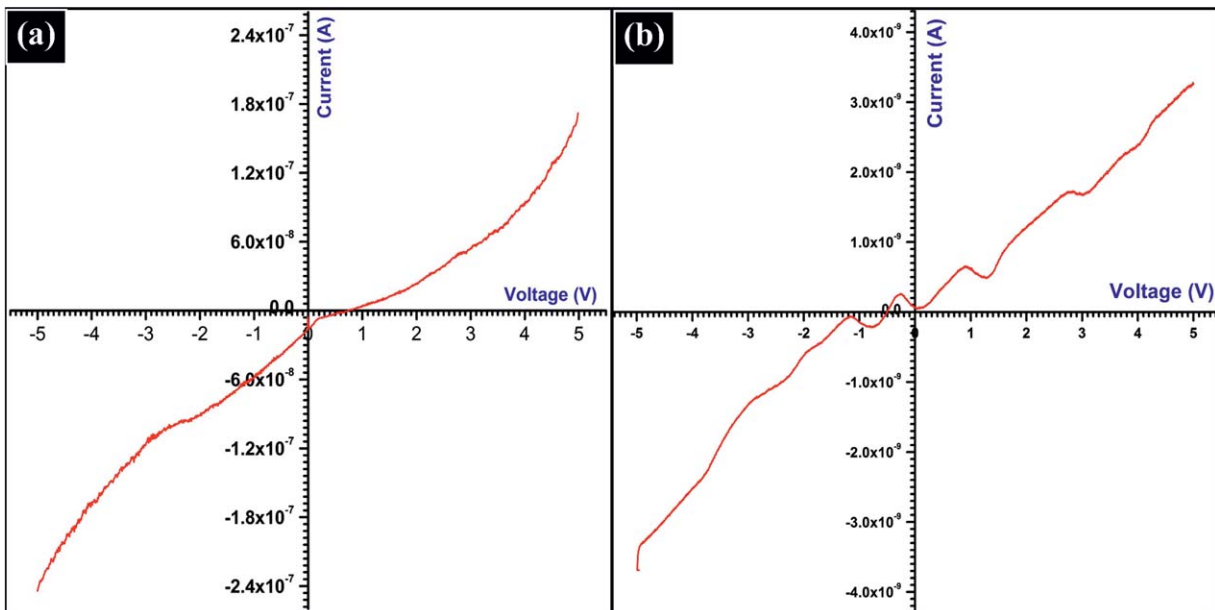

Fig. 7. (**a**) The I–V characteristic curve of the conventional MEMS device, (**b**) the I–V characteristic curve of the MEMS device with high resistivity. [Color figure can be viewed in the online issue, which is available at wileyonlinelibrary.com.]
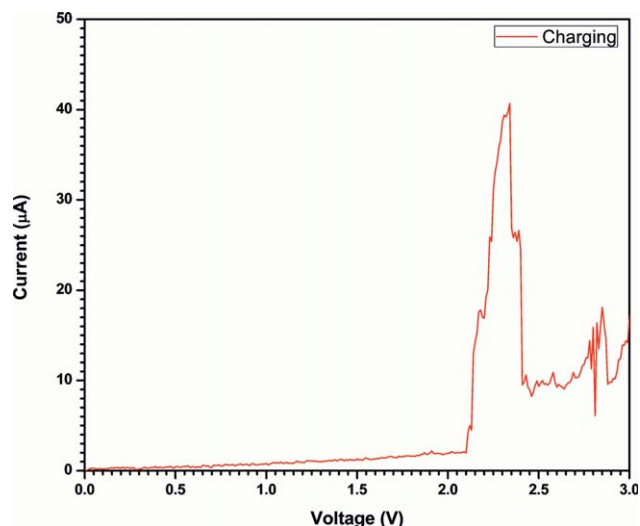
Fig. 8. I–V curve of the in situ electrochemical charging. [Color figure can be viewed in the online issue, which is available at wiley onlinelibrary.com.]

noticeably to the resistance. Therefore, we used IBID for contacting the sample, even though the metal contamination area is larger.

Leakage Current

Any leakage current through the MEMS device leads to a higher charging current and gradual loss of energy stored in the charged battery and thus to a faster discharge than expected. This leads to varying results of charging currents in in situ experiments. Therefore, it is important to have low leakage currents, especially for characterizing the charged state where it provides more time to perform additional TEM characterization. The IV curves of the standard MEMS (Protochips E-AEL11) devices and the new high resistance MEMS (Protochips E-AEK11) devices have been acquired using blank devices mounted in the Aduro TEM holder at a vacuum level of 10^{-7} mbar. A Keithley 2611 source meter and the Keithley control software has been used to perform voltage sweeps between -5 V and 5 V. The standard MEMS devices from Protochips have resistances of $\sim$30 MΩ (Fig. 7a)
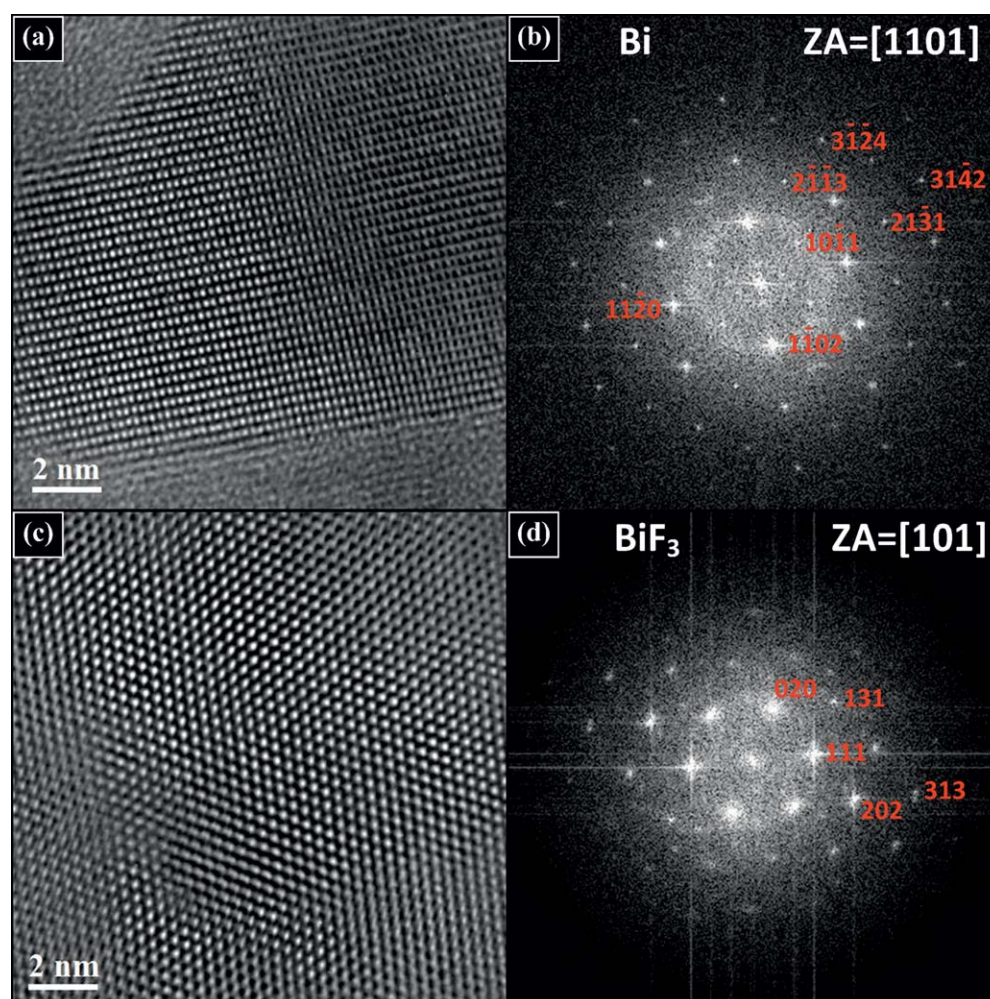

Fig. 9. (**a**) The HRTEM micrograph and the corresponding FFT of the as prepared cathode, (**b**) the HRTEM micrograph and the corresponding FFT of the cathode after charging. [Color figure can be viewed in the online issue, which is available at wileyonlinelibrary.com.]
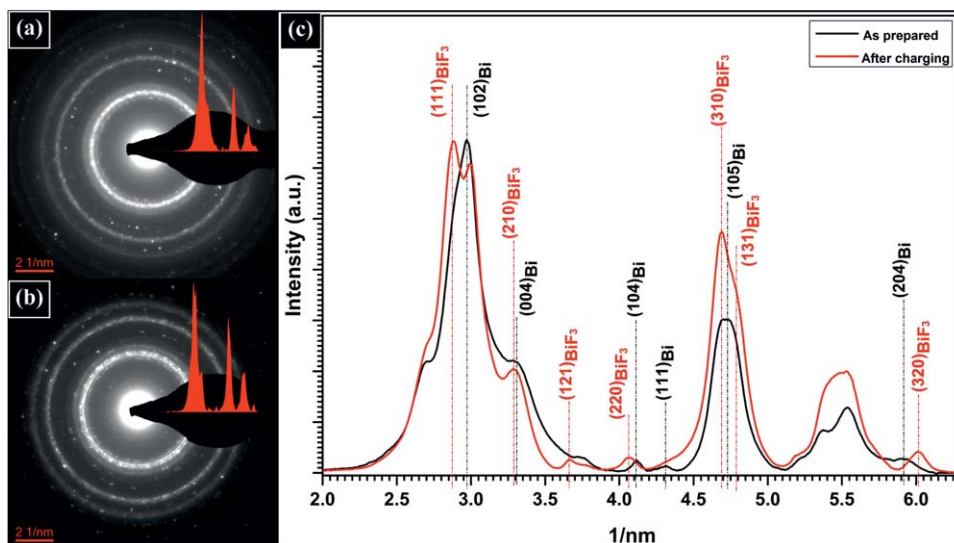
Fig. 10. (**a**) SAED pattern of the as-prepared cathode $(Bi + La_{0.9}Ba_{0.1}F_{2.9} + C)$, (**b**) SAED pattern of the charged cathode $(BiF_3 + (Bi) + La_{0.9}Ba_{0.1}F_{2.9} + C)$, (**c**) the profile of the SAED patterns of the cathode before and after charging. [Color figure can be viewed in the online issue, which is available at wileyonlinelibrary.com.]

while, the new high resistance MEMS devices have resistances of ~ 1.5 GΩ leading to leakage currents ~ 2 nA at 3 V (Fig. 7b).

Electrochemical Performance of the Micron-sized Battery

Before performing the sample preparation for the in situ studies, the as-prepared components of the fluoride ion battery and ex situ cycled fluoride ion batteries were investigated to study the effect of the electron beam on the material. The results confirmed that the fluoride ion battery materials are stable under normal operation conditions, so that standard TEM techniques can be used for imaging and analytical TEM of the fluoride ion battery components. No damage can be observed for the electrode materials, while for the electrolyte, the critical dose where the $(002)LaF_3$, $(\bar{1}20)LaF_3$, $(032)LaF_3$ reflections intensities started to decrease was 1100 e/nm^{2}s at 300 kV.

In addition, the effect of the electron beam current on the measured current in the electrochemical circuit was measured by positioning the electron beam in the TEM on the electron transparent thinned areas, thick areas and the Pt contacts of the MEMS device (Protochips E-AEK11). For these measurements, a DC voltage between 0 and 180 mV was applied on the micron-size battery and the corresponding areas illuminated by the electron beam. The thickness of the thinned and thick areas was ~ 100 nm and 6 μm, respectively, while the thickness of the Pt contacts was around 4 μm. The measured effect of the electron beam during charging was ~ 0.5 nA, 1–2 nA, and 1–1.5 nA on the electron transparent thinned areas, thick areas and the Pt contacts respectively. They were found to be negligible compared to the operating currents of the fluoride ion battery.

All of the above indicates that the all-solid-state fluoride battery is a suitable system for demonstration of in situ TEM electrochemical measurements. As a first test, the electrochemical performance of a cathode half-cell fluoride ion battery, consisting of $La_{0.9}Ba_{0.1}F_{2.9}$ as electrolyte and $Bi + La_{0.9}Ba_{0.1}F_{2.9} + C$ as a cathode, has been biased inside an aberration corrected FEI Titan 80-300 TEM using a Protochips Aduro holder and a Keithley 2611 source meter.

The cathode half-cell was charged from 0 to 3 V over a period of 1 h. The charging led to the formation of BiF_3 at the cathode and a reduction of the $La_{0.9}Ba_{0.1}F_{2.9}$ in the electrolyte forming a full cell during the reaction. Figure 8 shows the I–V charging curve of the half-cell measured in situ in the TEM. The structural and chemical modifications of the cathode and electrolyte during charging were characterized using BF-TEM and selected area electron diffraction (SAED). From the BF-TEM images and SAED studies of the cathode (Figs. 9 and 10), the formation of BiF_3 could be confirmed, which was absent in the as-prepared (discharged) state. In addition, the expected change in the electrolyte during charging could be observed, where reflections corresponding to La and Ba were detected after charging. The combination of the CV measurements and the observed structural changes prove the local electrochemical reaction of the battery. Thus, this method of sample preparation results in a working micron-size all-solid state battery for in situ TEM studies, overcoming the aforementioned challenges to a great extent.

CONCLUSION

Starting from a powder based all solid-state fluoride ion battery; an optimized FIB based approach to prepare a micron-sized battery for in situ TEM studies has been shown in this work. This preparation has been optimized for in situ TEM characterization by overcoming major challenges such as porosity, metal contamination and redeposition, leakage currents and contact resistance. The sample preparation was performed as a large area cross-section lift-out, which has been transferred onto electro-contacting MEMS

(Protochips E-AEK11) devices. The sample geometry and the contacting of the micron-sized battery on the MEMS (Protochips E-AEK11) device have been optimized to minimize the metal contamination and to maintain reasonable conductivity of the contacts. The successful battery preparation has been demonstrated for a half-cell fluoride ion battery ($La_{0.9}Ba_{0.1}F_{2.9}$//$Bi + La_{0.9}Ba_{0.1}F_{2.9} + C$) showing the fluorination of Bi to BiF_3 and simultaneously the reduction of $La_{0.9}Ba_{0.1}F_{2.9}$ to La and Ba during charging, following the charging process by CV and by electron diffraction.

ACKNOWLEDGMENT

REFERENCES

Abellan P, Woehl TJ, Parent LR, Browning ND, Evans JE, Arslan I. 2014. Factors influencing quantitative liquid (scanning) transmission electron microscopy. Chem Commun 50:4873–4880.

Beaulieu LY, Eberman KW, Turner RL, Krause LJ, Dahn JR. 2001. Colossal reversible volume changes in lithium alloys. Electrochem Solid-State Lett 4:A137–A141.

Belharouak I, Koenig GM, Amine K. 2011. Electrochemistry and safety of $Li_4Ti_5O_{12}$ and graphite anodes paired with $LiMn_2O_4$ for hybrid electric vehicle Li-ion battery applications. J Power Sources 196:10344–10350.

Bernal RA, Ramachandramoorthy R, Espinosa HD. 2015. Double-tilt in situ TEM holder with multiple electrical contacts and its application in MEMS-based mechanical testing of nanomaterials. Ultramicroscopy 156:23–28.

Bhattacharyya R, Key B, Chen H, Best AS, Hollenkamp AF, Grey CP. 2010. In situ NMR observation of the formation of metallic lithium microstructures in lithium batteries. Nat Mater 9:504–510.

Botman A, Hesselberth M, Mulders JJL. 2008. Investigation of morphological changes in platinum-containing nanostructures created by electron-beam-induced deposition. J Vacuum Sci Technol B 26: 2464–2467.

Brunel D, Troadec D, Hourlier D, Deresmes D, Zdrojek M, Mélin T. 2011. Characterization of ion/electron beam induced deposition of electrical contacts at the sub-μ scale. Microelectron Eng 88:1569–1572.

Chen D, Indris S, Schulz M, Gamer B, Mönig R. 2011. In situ scanning electron microscopy on lithium-ion battery electrodes using an ionic liquid. J Power Sources 196:6382–6387.

David L, Reddy TB. 2001. Handbook of Batteries. Third Edition. McGraw-Hill Companies, Inc. 1–1454.

Duchamp M, Xu Q, Dunin-Borkowski RE. 2014. Convenient preparation of high-quality specimens for annealing experiments in the transmission electron microscope. Microsc Microanal 20:1638–1645.

Fell CR, Chi M, Meng YS, Jones JL. 2012. In situ X-ray diffraction study of the lithium excess layered oxide compound $Li[Li_{0.2}Ni_{0.2}Mn_{0.6}]O_2$ during electrochemical cycling. Solid State Ionics 207:44–49.

Fernández-Pacheco A, De Teresa JM, Córdoba R, Ibarra MR. 2009. Metal-insulator transition in Pt-C nanowires grown by focused-ion-beam-induced deposition. Phys Rev B 79:174204(1–12).

Gu M, Parent LR, Mehdi BL, Unocic RR, McDowell MT, Sacci RL, Xu W, Connell JG, Xu P, Abellan P, Chen X, Zhang Y, Perea DE, Evans JE, Lauhon LJ, Zhang J, Liu J, Browning ND, Cui Y, Arslan I, Wang C. 2013. Demonstration of an electrochemical liquid cell for operando transmission electron microscopy observation of the lithiation/delithiation behavior of Si nanowire battery anodes. Nano Letters 13:6106–6112.

Han X, Ouyang M, Lu L, Li J. 2014. Cycle life of commercial lithium-ion batteries with lithium titanium oxide anodes in electric vehicles. Energies 7:4895–4909.

Hardwick LJ, Holzapfel M, Novák P, Dupont L, Baudrin E. 2007. Electrochemical lithium insertion into anatase-type TiO_2: an in situ Raman microscopy investigation. Electrochim Acta 52:5357–5367.

Hardwick LJ, Ruch PW, Hahn M, Scheifele W, Kötz R, Novák P. 2008. In situ Raman spectroscopy of insertion electrodes for lithium-ion batteries and supercapacitors: first cycle effects. J Phys Chem Solids 69:1232–1237.

Harks PPRML, Mulder FM, Notten PHL. 2015. In situ methods for Li-ion battery research: a review of recent developments. J Power Sources 288:92–105.

Hatchard TD, Dahn JR. 2004. In situ XRD and electrochemical study of the reaction of lithium with amorphous silicon. J Electrochem Soc 151:A838–A842.

Hiroshima H, Komuro M. 1997. High growth rate for slow scanning in electron-beam-induced deposition. Jpn J Appl Phys 36:7686–7690.

Horváth E, Neumann PL, Tóth AL, Vázsonyi É, Koós AA, Horváth ZE, Fürjes P, Dücső C, Biró LP. 2006. Electrical characterization of tungsten nanowires deposited by focused ion beam (FIB). Nanopages 1:255–262.

Hoyle PC, Ogasawara M, Cleaver JRA, Ahmed H. 1993. Electrical resistance of electron beam induced deposits from tungsten hexacarbonyl. Appl Phys Lett 62:3043–3045.

Hoyle PC, Cleaver JRA, Ahmed H. 1994. Ultralow-energy focused electron beam induced deposition. Appl Phys Lett 64:1448–1450.

Huang JY, Zhong L, Wang CM, Sullivan JP, Xu W, Zhang LQ, Mao SX, Hudak NS, Liu XH, Subramanian A, Fan H, Qi L, Kushima A, Li J. 2010. In situ observation of the electrochemical lithiation of a single SnO_2 nanowire electrode. Science 330:1515–1520.

Jenkins DWK, Allen GC, Prewett PD, Heard PJ. 1999. Focused ion-beam assisted deposition of tungsten and carbon. J Phys Condens Matter 3:S199–S206.

Jublot M, Texier M. 2014. Sample preparation by focused ion beam micromachining for transmission electron microscopy imaging in front-view. Micron 56:63–67.

Kanzaki N, Wilhite P, Maeda S, Yamadal T, Yang CY. 2011. Contact improvement using E-beam and FIB deposited tungsten in carbon nanofiber interconnects. IEEE Nanotechnol Mater Dev Conference. Jeju, South Korea. 248–251.

Key B, Bhattacharyya R, Morcrette M, Seznéc V, Tarascon J, Grey CP. 2009. Real-time NMR investigations of structural changes in silicon electrodes for lithium-ion batteries. J Am Chem Soc 131: 9239–9249.

Key B, Morcrette M, Tarascon J-M, Grey CP. 2011. Pair distribution function analysis and solid state NMR studies of silicon electrodes for lithium ion batteries: Understanding the (de)lithiation mechanisms. J Am Chem Soc 133:503–512.

Koh YB, Garno K, Namba S. 1991. Characteristics of W films formed by ion beam assisted deposition. J Vacuum Sci Technol B 9:2648–2652.

Kuwano S, Fujita T, Pan D, Wang K, Chen M. 2008. TEM sample preparation for microcompressed nanocrystalline Ni. Mater Trans 49:2091–2095.

Langfischer H, Basnar B, Hutter H, Bertagnolli E. 2002. Evolution of tungsten film deposition induced by focused ion beam. J Vacuum Sci Technol A 20:1408–1415.

Leenheer AJ, Jungjohann KL, Zavadil KR, Sullivan JP, Harris CT. 2015. Lithium electrodeposition dynamics in aprotic electrolyte observed in situ via transmission electron microscopy. ACS Nano 9: 4379–4389.

Li J, Dahn JR. 2007. An in situ X-ray diffraction study of the reaction of Li with crystalline Si. J Electrochem Soc 154:A156–A161.

Li W, Warburton PA. 2007. Low-current focused-ion-beam induced deposition of three-dimensional tungsten nanoscale conductors. Nanotechnology 18:485305(1–5).

Li PG, Jin AZ, Tang WH. 2006. Pt/Ga/C and Pt/C composite nanowires fabricated by focused ion and electron beam induced deposition. Phys Status Solid (a) 203:282–286.

Li W, Fenton JC, Wang Y, McComb DW, Warburton PA. 2008. Tunability of the superconductivity of tungsten films grown by focused-ion-beam direct writing. J Appl Phys 104:093913(1–10).

Li W, Fenton JC, Cui A, Wang H, Wang Y, Gu C, McComb DW, Warburton PA. 2012. Felling of individual freestanding nanoobjects using focused-ion-beam milling for investigations of structural and transport properties. Nanotechnology 23:105301(1–10).

Lin J-F, Bird JP, Rotkina L, Bennett PA. 2003. Classical and quantum transport in focused-ion-beam-deposited Pt nanointerconnects. Appl Phys Lett 82:802–804.

Lin JF, Bird JP, Rotkina L, Sergeev A, Mitin V. 2004. Large effects due to electron-phonon-impurity interference in the resistivity of Pt/C-Ga composite nanowires. Appl Phys Lett 84:3828–3830.

Liu XH, Huang JY. 2011. In situ TEM electrochemistry of anode materials in lithium ion batteries. Energy Environ Sci 4:3844–3860.

Liu XH, Liu Y, Kushima A, Zhang S, Zhu T, Li J, Huang JY. 2012. In situ TEM experiments of electrochemical lithiation and delithiation of individual nanostructures. Adv Energy Mater 2:722–741.

Long BR, Chan MKY, Greeley JP, Gewirth AA. 2011. Dopant modulated Li insertion in Si for battery anodes: Theory and experiment. J Phys Chem C 115:18916–18921.

Mansour AN, Badway F, Yoon W-S, Chung KY, Amatucci GG. 2010. In situ X-ray absorption spectroscopic investigation of the electrochemical conversion reactions of CuF_2–MoO_3 nanocomposite. J Solid State Chem 183:3029–3038.

Marsh RA, Vukson S, Surampudi S, Ratnakumar BV, Smart MC, Manzo M, Dalton PJ. 2001. Li ion batteries for aerospace applications. J Power Sources 97/98:25–27.

Mayer J, Giannuzzi LA, Kamino T, Michael J. 2007. TEM sample preparation and FIB-induced damage. MRS Bull 32:400–407.

Melngailis J. 1991. Focused ion beam induced deposition—A review. In: SPIE Vol. 1465 Electron-Beam, X-Ray, and Ion-Beam Submicrometer Lithographies for Manufacturing, pp. 36–49.

Meng YS, McGilvray T, Yang M-C, Gostovic D, Wang F, Zeng D, Zhu Y, Graetz J. 2011. In situ analytical electron microscopy for probing nanoscale electrochemistry. Electrochem Soc Interface Fall 2011: 49–53.

Miller BK, Barker TM, Crozier PA. 2015. Novel sample preparation for operando TEM of catalysts. Ultramicroscopy 156:18–22.

Moorthy SKE, Goff GL, Viret M, Kociak M. 2013. In situ break-junction sample holder for transmission electron microscopy. Eur Phys J Appl Phys 64:31001(p1–p4).

Mulders JJL. 2014. Purity and resistivity improvements for electron-beam-induced deposition of Pt. Appl Phys A 117:1697–1704.

Nan LK, Lung LM. 2013. Study of FIB milling induced damage and contamination on ex-situ lift-out TEM specimen and methodology to reduce the artifacts. Proceedings of the International Symposium on the Physical and Failure Analysis of Integrated Circuits, IPFA 404–407.

Nishizawa A, Kallo J, Garrot O, Weiss-Ungethüm J. 2013. Fuel cell and Li-ion battery direct hybridization system for aircraft applications. J Power Sources 222:294–300.

Nonaka T, Okuda C, Ukyo Y, Okamoto T. 2001. In situ XAFS study on cathode materials for lithium-ion batteries. J Synchrotron Radiat 8:869–871.

Obrovac MN, Christensen L. 2004. Structural changes in silicon anodes during lithium insertion/extraction. Electrochem Solid-State Lett 7:A93–A96.

Orsini F, Du Pasquier A, Beaudoin B, Tarascon JM, Trentin M, Langenhuizen N, De Beer E, Notten P. 1998. In situ scanning electron microscopy (SEM) observation of interfaces within plastic lithium batteries. J Power Sources 76:19–29.

Petibon R, Li J, Sharma N, Pang WK, Peterson VK, Dahn JR. 2015. The use of deuterated ethyl acetate in highly concentrated electrolyte as a low-cost solvent for in situ neutron diffraction measurements of Li-ion battery electrodes. Electrochim Acta 174:417–423.

Platen KTK, Buchmann L-M, Petzold H-C, Brünger WH. 1992. Electron-beam induced tungsten deposition: Growth rate enhancement and applications in microelectronics. J Vac Sci Technol B 10:2690–2694.

Prestigiacomo M, Roussel L, Houel A, Sudraud P, Bedu F, Tonneau D, Safarov V, Dallaporta H. 2004. Studies of structures elaborated by focused ion beam induced deposition. Microelectron Eng 76:175–181.

Purvins A, Sumner M. 2013. Optimal management of stationary lithium-ion battery system in electricity distribution grids. J Power Sources 242:742–755.

Ramdon S, Bhushan B, Nagpure SC. 2014. In situ electrochemical studies of lithium-ion battery cathodes using atomic force microscopy. J Power Sources 249:373–384.

Reddy MA, Fichtner M. 2011. Batteries based on fluoride shuttle. J Mat Chem 21:17059–17062.

Reguer A, Bedu F, Tonneau D, Dallaporta H, Prestigiacomo M, Houel A, Sudraud P. 2008. Structural and electrical studies of conductive nanowires prepared by focused ion beam induced deposition. J Vacuum Sci Technol B 26:175–180.

Roberts M, Biendicho JJ, Hull S, Beran P, Gustafsson T, Svensson G, Edström K. 2013. Design of a new lithium ion battery test cell for in-situ neutron diffraction measurements. J Power Sources 226: 249–255.

Rongeat C, Reddy MA, Diemant T, Behm RJ, Fichtner M. 2014. Developement of new anode composite materials for fluoride ion batteries. J Mater Chem A 2:20861–20872.

Rosso M, Brissot C, Teyssot A, Dollé M, Sannier L, Tarascon J-M, Bouchet R, Lascaud S. 2006. Dendrite short-circuit and fuse effect on Li/polymer/Li cells. Electrochim Acta 51:5334–5340.

Sagane F, Shimokawa R, Sano H, Sakaebe H, Iriyama Y. 2013. In-situ scanning electron microscopy observations of Li plating and stripping reactions at the lithium phosphorus oxynitride glass electrolyte/Cu interface. J of Power Sources 225:245–250.

Shao M. 2014. In situ microscopic studies on the structural and chemical behaviors of lithium-ion battery materials. J Power Sources 270:475–486.

Sharma N, Peterson VK, Elcombe MM, Avdeev M, Studer AJ, Blagojevic N, Yusoff R, Kamarulzaman N. 2010. Structural changes in a commercial lithium-ion battery during electrochemical cycling: An in situ neutron diffraction study. J Power Sources 195:8258–8266.

Smith K, Earleywine M, Wood E, Neubauer J, Pesaran A. 2012. Comparison of Plug-In Hybrid Electric Vehicle Battery Life Across Geographies and Drive Cycles. SAE International doi:10.4271/2012-01-0666.

Su Q, Du G, Zhang J, Zhong Y, Xu B, Yang Y, Neupane S, Kadel K, Li W. 2013a. In situ transmission electron microscopy investigation of the electrochemical lithiation-delithiation of individual Co_9S_8/co-filled carbon nanotubes. ACS Nano 7:11379–11387.

Su Q, Chang L, Zhang J, Du G, Xu B. 2013b. In situ TEM observation of the electrochemical process of individual CeO_2/graphene anode for lithium ion battery. J Phys Chem C 117:4292–4298.

Takami N, Inagaki H, Tatebayashi Y, Saruwatari H, Honda K, Egusa S. 2013. High-power and long-life lithium-ion batteries using lithium titanium oxide anode for automotive and stationary power applications. J Power Sources 244:469–475.

Teresa JM, Córdoba R, Fernández-Pacheco A, Montero O, Strichovanec P, Ibarra MR. 2009. Origin of the difference in the resistivity of as-grown focused-ion- and focused-electron-beam-induced Pt nanodeposits. J Nanomater 2009:936863(1–11).

Tham D, Nam C-Y, Fischer JE. 2006. Microstructure and composition of focused-ion-beam-deposited Pt contacts to GaN nanowires. Adv Mater 18:290–294.

Uhlig T, Heumann M, Zweck J. 2003. Development of a specimen holder for in situ generation of pure in-plane magnetic fields in a transmission electron microscope. Ultramicroscopy 94:193–196.

Utke I, Hoffmann P, Melngailis J. 2008. Gas-assisted focused electron beam and ion beam processing and fabrication. J Vacuum Sci Technol B 26:1197–1276.

Vaz AR, Silva MM, Leon J, Moshkalev SA, Swart JW. 2008. Platinum thin films deposited on silicon oxide by focused ion beam: Characterization and application. J Mater Sci 43:3429–3434.

Wagner R. 2007. Chapter 9-Stationary applications. III. Lead-acid batteries for solar and wind energy storage. in: Industrial applications of batteries. From Cars to Aerospace and Energy Storage. First edition. Elsevier, Amsterdam, Netherlands. pp 497–545. doi: 10.1016/B978-044452160-6/50010-3.

Wang C-M. 2014. In situ transmission electron microscopy and spectroscopy studies of rechargeable batteries under dynamic operating conditions: A retrospective and perspective view. J Mater Res 30: 326–339.

Warner J. 2015. Chapter 15—Lithium-ion battery applications. The Handbook of Lithium-Ion Battery Pack Design 177–209. doi: 10.1016/B978-0-12-801456-1.00015-4.

Woehl TJ, Evans JE, Arslan I, Ristenpart WD, Browning ND. 2012. Direct in situ determination of the mechanisms controlling nanoparticle nucleation and growth. ACS Nano 8:8599–8610.

Xie J, Tu F, Su Q, Du G, Zhang S, Zhu T, Cao G, Zhao X. 2014. In situ TEM characterization of single PbSe/reduced-graphene-oxide nanosheet and the correlation with its electrochemical lithium storage performance. Nano Energy 5:122–131.

Xu T, Wang W, Gordin ML, Wang D, Choi D. 2010. Lithium-ion batteries for stationary energy storage. JOM 62:24–30.

Yamamoto K, Iriyama Y, Asaka T, Hirayama T, Fujita H, Fisher CAJ, Nonaka K, Sugita Y, Ogumi Z. 2010. Dynamic visualization of the electric potential in an all-solid-state rechargeable lithium battery. Angew Chem. (International Ed. in English) 49:4414–4417.

Zamfir MR, Nguyen HT, Moyen E, Lee YH, Pribat D. 2013. Silicon nanowires for Li-based battery anodes: A review. J Mater Chem A 1:9566–9586.